Study of the Implementation of Dual Energy Decomposition in a Real Digital Radiography System

C. de Molina[1,2], I. García[1,2], M.Desco[1,2,3], M. Abella[1,2]

[1] Dept. Bioingeniería e Ingeniería Aeroespacial, Universidad Carlos III de Madrid, España

[2] Instituto de Investigación Sanitaria Gregorio Marañón, Madrid, España

[3] Centro de investigación en red en salud mental (CIBERSAM), Madrid, España

Abstract

Dual energy decomposition in Digital Radiography consists on the extraction of two tissues (frequently bone and soft tissue) from two acquisitions at two different source voltages (low and high energy). Most of the proposed methods in the literature do not explore the practical considerations that have to be considered in order to incorporate the procedure into a real digital radiography system. In this work, we study practical issues such as the optimal design of the calibration phantom and possible problems in calibration process derived from the positioning of the phantom and the mechanical misalignments of the system. As a result, we define a complete protocol to incorporate dual energy decomposition into a Digital Radiography system.

1. Introduction

Dual energy decomposition, based on the acquisition of two images at different voltages, enables the characterization of different tissues (frequently bone and soft tissue). Its clinical benefit has been demonstrated in several applications such as the identification of lung lesions hidden by the ribs. Figure 1 shows an example of the low and high energy data and the soft tissue and bone images extracted.

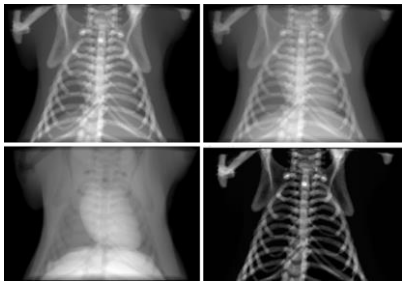

Figure 1. *Top: low (left) and high (high) energy radiography. Bottom: soft tissue (left) and bone (right) images after dual energy decomposition*

Several methods have been proposed in the literature. In 1976, Alvarez et al [1, 2] set the basis of this technique by modeling the high and low energy data using polynomial functions and solving the resulting non-linear system with the Newton-Raphson iterative method. In [3, 4], the authors presented an alternative direct approximation, modeling directly the resulting images in order to avoid iterative algorithms. Both methods require a previous calibration with different combinations of bone and soft tissue to obtain the model parameters.

Another different model was proposed in [5], based on the so-called iso-transmission lines, that models the data as straight lines instead of third order polynomial functions. In [6], the authors proved that the use of conic and cubic equations could accelerate the calibration significantly. The problem with these two methods is that they imply a more complex formulation.

Most of the proposed methods describe the theory fundamentals but do not address any of the practical issues of implementation in a real system. In this work, we describe a suitable algorithm for a Digital Radiography system, design the optimal calibration phantom and study the effects of errors in the procedure with simulations. As a result, we define a new complete protocol for incorporating dual energy decomposition into a Digital Radiography system and solving the practical problems.

2. Design of the protocol for dual energy decomposition

2.1. Digital Radiography System

We have studied the practical considerations by simulating a clinical digital radiography system with the geometry described in Figure 2. For this purpose, we used a simulation tool developed by our group, implemented in CUDA language and accelerated using parallel processing in GPUs.

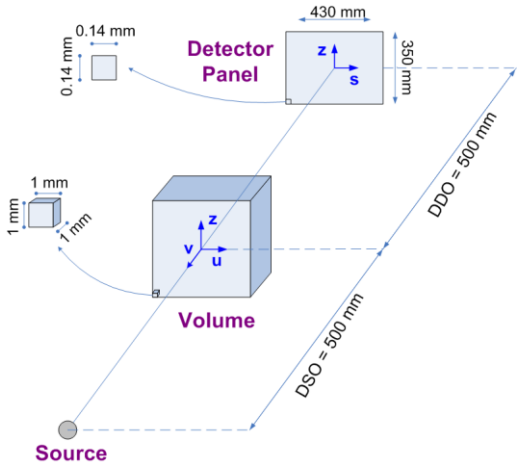

Figure 2. *Scheme of the radiography system geometry*

For a polychromatic source the measured data for the low and high acquisitions (I_L and I_H respectively) are modeled with the Beer's equation:

$$\begin{cases} I_L = \int I_{0,L}(\varepsilon_L)\cdot e^{-(t_S m_S(\varepsilon_L)+t_B m_B(\varepsilon_L))}d\varepsilon & (1) \\ I_H = \int I_{0,H}(\varepsilon_H)\cdot e^{-(t_S m_S(\varepsilon_H)+t_B m_B(\varepsilon_H))}d\varepsilon & (2) \end{cases}$$

where $I_{0,L}, I_{0,H}$ are the intensities of the X-ray beam emitted from the source for low (L) and high energy (H); and (ρ_S, ρ_B) and $(m_S(\varepsilon), m_B(\varepsilon))$ are the physical density and mass attenuation coefficients for soft tissue (S) and bone (B) respectively. The mass attenuation coefficient for each material depends on the photon energy (ε) and has been extracted from the National Institute of Standard and Technology (NIST) data; the polychromatic spectra of 70 KVp (low) and 140 KVp (high) have been simulated using the TASMIP model [8]. t_S and t_B, the quantities of interest that will form the images of bone and soft tissue (see Figure 1, bottom) are the total thickness of bone and soft tissue traversed along the path L followed by the X-ray:

$$t_S = \int_L \rho_S dl\,,\; t_B = \int_L \rho_B dl \qquad (3)$$

Preliminary tests were done with a public domain 3D mouse atlas (http://neuroimage.usc.edu/neuro/Digimouse) which allows for a good definition of a complete thorax with four different soft tissues and bone. In order to translate to a clinical system we adapt it to a human thorax both in size (40.5x17.5x28.5 cm) and densities (values extracted from [9]).

2.2. Dual energy algorithm

From equations (1) and (2) we can see that is not possible to obtain the t_S and t_b directly because of the non-linear relationship between them and the data.

We have implemented the direct approximation method [3, 4] for dual energy decomposition because the calibration procedure is simple and fast, and the decomposition is direct, avoiding the need of an iterative algorithm. Instead of solving the non-linear system (1) and (2), this method approximates the soft tissue and bone traversed thicknesses (t_s and t_B) separately using a model based on third order polynomic functions:

$$t_s = a_0 + a_1 d_H + a_2 d_L + a_3 d_H d_L + a_4 d_H^2 + a_5 d_L^2 + a_6 d_H^3 + a_7 d_L^3 \quad (4)$$

$$t_B = b_0 + b_1 d_H + b_2 d_L + b_3 d_H d_L + b_4 d_H^2 + b_5 d_L^2 + b_6 d_H^3 + b_7 d_L^3 \quad (5)$$

where t_S and t_B are the unknowns (soft tissue and bone images) and $d_L = \ln\left(I_L / I_0\right)$, $d_H = \ln\left(I_H / I_0\right)$ are the high and low energy log measured data. The polynomial coefficients a_i and b_i are obtained in a calibration step that consists on the acquisition of different known combinations of two materials of interest with high and low energy (similar to soft tissue and bone): d_H and d_L in the equations system. The thicknesses of bone and soft tissue equivalent materials (t_S and t_B in the equations) are simulated by projecting the calibration phantom. This requires to include in the simulator the exact geometry of the system and positioning of the phantom in order to estimate the X-ray trajectories. Figure 3 shows these images for the calibration phantom depicted in Figure 4. Once we have t_S, t_B, d_H and d_L, the calibration coefficients a_i and b_i are found by solving the non-linear system using least squares and saved in a calibration file.

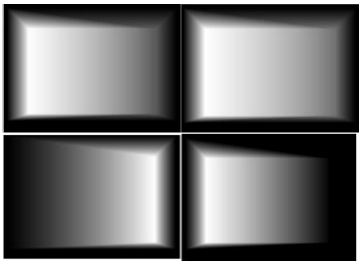

Figure 3. *Top: low (left) and high (right) log-data of the phantom. Bottom: t_S and t_B images of the phantom*

For any dual energy study, we can obtain soft tissue and bone, t_S and t_B, images like those in bottom panel of Figure 1 from the equations in the direct form (4) and (5).

2.3. Design of the calibration phantom

To design the optimal calibration phantom we need to decide the material and the size/shape. The size and shape will influence the sampling of material thicknesses traversed (t_S and t_B). The selected shape is that shown in Figure 4, where the plane formed by Dim_u and Dim_z is stitched to the detector plane, as suggested in [4], which gives a good sampling of different thicknesses and is easy to manufacture

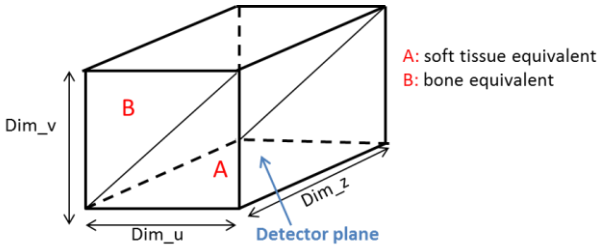

Figure 4. *Scheme of the calibration phantom*

In order to find the appropriate dimensions for the system under study, we have simulated several calibration phantoms with different dimensions from 10.8 to 27 cm (square and rectangular ones). The maximum thickness was selected taking into account that we need to reach the maximum thickness of soft tissue (~20 cm) and bone (~6 cm) in a human body, but also using a portable phantom that does not exceed the detector dimensions. We chose a phantom with both parts equal because it is easier to assemble.

In Figure 5 we present the histogram of traversed thickness for the different calibration phantoms.

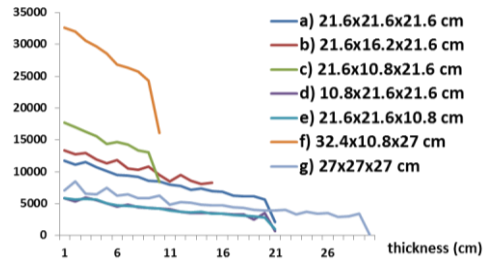

Figure 5. *Histogram of the thicknesses of the phantoms with different dimensions*

A planar histogram means that the sampling is constant along the different thicknesses. Due to the shape of the phantom, Dim_v (see Figures 3 and 4) gives the maximum thickness; Dim_u and Dim_z provide the total number of thicknesses. Based on our results finally selected a phantom of 27 x 27 x 27 cm.

Regarding the two materials of the phantom, the a priori intuitive idea is that they should be similar in density and mass attenuation coefficient to soft tissue and bone. We have simulated the acquisitions of different phantoms made of different materials: soft tissue, water, PMMA and A-150 Tissue-Equivalent Plastic for the case of the soft tissue-material; and bone, Polytetrafluoroethylene ("Teflon"), B-100 Bone-Equivalent Plastic and aluminum for the bone equivalent material.

Although some materials may seem to be more appropriate because their physical density is more similar to those of soft tissue and bone, the most suitable are the ones which present a mass attenuation coefficient curve nearest to the original one.

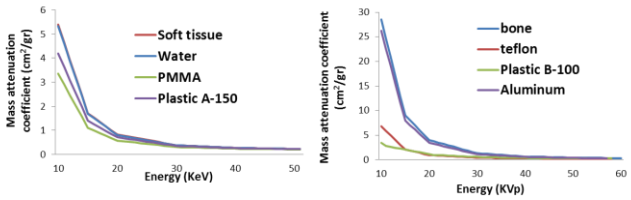

Figure 6.*Mass attenuation coefficients of the different studied materials for the energy range where the differences are significant (1-60KeV)*

In the case of equivalent soft tissue, the mass attenuation curves of the different materials (PMMA and A-150) are very close to the soft tissue/water ones (Figure 6, left). Based on the mass attenuation curves, it seems that there are no significant differences, but in the bone image (t_B) we can appreciate some areas where the soft tissue has not been subtracted. To quantify this, we measured the region of interest (ROI) depicted in Figure 7 where should be background in the bone image. The bone image with less soft tissue is the one made with the plastic A-150 phantom, 1.16 vs. 1.9 for the PMMA case. That indicates that the plastic A-150 is a material more appropriated for the dual energy subtraction.

Regarding the bone equivalent material, the differences between the different materials (bone, Teflon, plastic B-100 and aluminum) both in mass attenuation curves as in the decomposed images are significant (Figure 6, right).

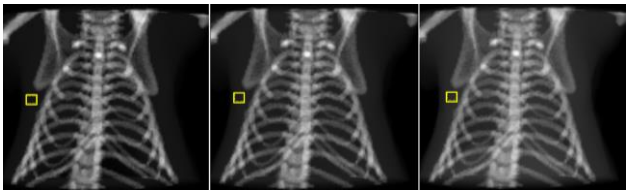

Figure 7. *Bone tissue images extracted with the implemented algorithm when the soft tissue equivalent material of the calibration phantom is water (left), plastic A-150 (center) and PMMA (right). The yellow square indicates the measured ROI: 0.7(left), 1.16 (center) and 1.9 (right).*

From these results, we can see that a possible phantom could be made of plastic A-150 (soft tissue equivalent material) and aluminum (bone tissue equivalent material) to perform the dual energy decomposition properly.

2.4. Error of estimation of material thicknesses

As explained above, the estimation of the material thicknesses is made by simulating the projection of the calibration phantom. In a real system, the geometry varies with respect to the ideal case due to tolerances of manufacturing and mechanical misalignments. Another source of error is the manual positioning: we need to know the exact position of the calibration phantom in order to estimate the material thicknesses by simulation. The discrepancies between the real data and the simulation will produce errors in the estimation of the equivalent soft tissue and bone thicknesses (t_S and t_B). Since these errors in the calibration may influence the results, we have studied their effect in the resulting images with the dual energy decomposition algorithm (Figure 8).

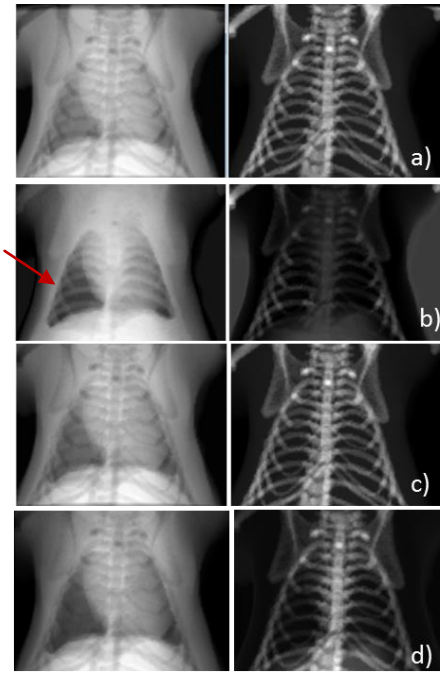

Figure 8. *Soft tissue and Bone images obtained when the estimation of the thicknesses of the calibration phantom in the ideal case (a) and with errors of 20 mm in the u-axis (b), 20 mm in the z-axis (c) and 45 mm in the origin to detector distance (d)*

We have simulated errors shifts in the u-axis (5, 10, 20 mm) and z-axis (5, 10, 20 mm) and in the origin to detector distance (5, 10, 20 40, 50, 55, 75, 100 mm).

The most critical direction is along u-axis because the change of thickness traversed when moving along the phantom diagonal is faster. In Figure 8 (a) we show an ideal case knowing the complete geometry and positioning of the phantom and in (b), the results when the phantom is moved 20 mm in the critical direction (u-axis). We can see that the decomposition does not work well for this value because the ribs appear in the soft tissue image (red arrow). For lower values, the differences with respect to the ideal case are difficult to appreciate visually.

Due to the phantom design, errors in the calculated thicknesses are not so sensitive to movements along the z-axis. In (c), the images when the phantom is moved 20 mm in this direction show that this effect is not noticeable.

Finally, in (d) we can see the effect of an error in the origin to detector distance of 45 mm. For higher values we see the liver in the bone image and from 60 mm the ribs do not appear complete. Errors lower that 45 mm in the origin to detector distance do not seem to affect the dual energy decomposition.

2.5. Effect of the bed table

Finally, considering those systems in which there is a table bed (not removable) on top of the detector, we have studied if the additional amount of bed material affects the estimation of material thicknesses.

To this end, we have simulated a standard table with a thickness of 50 mm made of carbon fiber (2 mm equivalent Aluminum) in order to see how an additional material not taken into account may affect the estimation of the thicknesses.

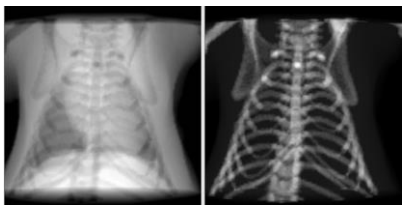

Figure 9. *Soft tissue and bone images decomposition when there is a table bed of 2 mm equivalent Aluminum.*

As we can see in Figure 9, the soft tissue and bone images are close to the original ones. After quantifying the images we have verified that the bed material only affects in the background values (0.077 vs 0.018 without bed) but not in the decomposition because the bed is very thin respect to the calibration phantom.

3. Conclusions

We have designed a new calibration protocol for dual energy decomposition in a Digital Radiography system, including the implementation of a suitable algorithm and studied technical considerations such as the optimal design of the phantom calibration, the error of the estimation of material thicknesses and the bed effect in the calibration procedure.

The selected algorithm is the direct approximation, based on the modeling of the desired data with third order polynomials, which needs a previous calibration. Tests have shown that the materials of the calibration phantom should be selected in such a way that its mass attenuation coefficient is similar to the tissues of interest, but the physical density is not so important. This is the case of the equivalent bone material where the aluminum has a higher density (2.7 gr/cm^3) vs. the plastic B-100 density (1.45 gr/cm^3) nearest to the ribs bone (1.48 gr/cm^3).

On the other hand, the acceptable errors of manual positioning are around 10 mm and 40 mm in the u and z axis respectively. The effect of error in u-axis is higher because it corresponds to the direction where the traversed thicknesses change more in the designed phantom. Future work includes the study of positioning of the phantom using guides to improve these error tolerances of the phantom positioning.

Errors in the origin to detector distance due to tolerances in the scanner manufacturing do not affect the result if they are below 45 mm. Finally, the material bed does not affect the quality of the result.

Aknowledgement

This work was partially funded by projects IPT-2012-0401-300000, TEC2011-28972-C02-01, TEC2013-48251-C2-1-R, and TEC2013 47270-R from Spanish Ministerio de Ciencia e Innovación.

References

[1] Alvarez, R.E. and A. Macovski, Energy-selective reconstruction in x-ray computerized tomography. Phys. Med. Biol., 1976. 21(5): p. 733–44.

[2] Lehmann, L.A., R.E. Alvarez, A. Macovski, W.R. Brody, N.J. Pelc, S.J. Riederer and A.L. Hall, Generalized image combinations in dual KVP digital radiography. Phys. Med. Biol., 1976. 21(5): p. 733–44.

[3] Heinzerling, J. and Schlindwein, M., Non-Linear Techniques in Multi-Spectral X-Ray Imaging. IEEE Transactions on Nuclear Science., 1980. 27(2)

[4] Brody, W.R., G. Butt, A. Hall and A. Macovski, A method for selective tissue and bone visualization using dual-energy scanned projection radiography. Medical Physics,1981. 8: p. 659-667.

[5] Chuang K.S. and H.K. Huang, Comparison of four dual energy image decomposition methods. Phys.Med. Biol,1988. 33 (4): p.4-466.

[6] Cardinal H.N. and A. Fenster, An accurate method for direct dual-energy calibration and decomposition. Medical Physics, 1990. 17 (3): p.327-341.

[7] Noh, J., J.A. Fessler and P.E. Kinahan, Statistical Sinogram Restoration in Dual-Energy CT for PET Attenuation Correction. IEEE Transactions of Medical Imaging, 2009. 28(11): p. 1688 - 1702.

[8] Siewerdsen , J.H., A.M. Waese, D.J. Moseley, S. Richard, and D.A. Jaffray, Spektr: A computational tool for x-ray spectral analysis and imaging system optimization. Medical Physics, 2004. 31: p. 3057-3067.

[9] Schneider U., E. Pedroni and A. Lomax, The calibration of CT Hounsfield units for radiotherapy treatment planning, Physics in Medicine and Biology, 1996, 41(1): p. 111-124